Extreme variation in fatigue: Laser powder bed fusion fatigue life prediction and dependence on build volume location in 17-4 stainless steel

Jaime Berez[a,*], Luke Sheridan[b], Christopher Saldaña[a]
[a]*George W. Woodruff School of Mechanical Engineering, Georgia Institute of Technology, 801 Ferst Dr., Atlanta, GA 30332, USA*
[b]*Air Force Research Laboratory, Aerospace Systems Directorate, Turbine Engine Structural Integrity Branch, 213 Eighth St., Rm 136, Wright Patterson AFB, Dayton, OH, USA*
Contact: j.berez@gatech.edu (J.B.)*, luke.sheridan.1@us.af.mil (L.S.), christopher.saldana@me.gatech.edu (C.S.)
*Corresponding author

Abstract

Laser powder bed fusion (LPBF), a metal additive manufacturing technology, is well-suited for design optimization but fatigue life is limited by manufacturing defects. In this work, 17-4 stainless steel components were manufactured in densely populated build volumes, simulating at-scale LPBF production. Tests revealed extreme variability in fatigue life data, analyzed via rigorous statistical tools. The El-Haddad model, modified for finite-life, enabled defect-based life prediction. Specimen location within the build volume correlated to life, which was heteroscedastic. Investigating defect concentration over the build volume explained typical life and scatter. These findings argue for qualification approaches which acknowledge high material lot variability.

Keywords: laser powder bed fusion; additive manufacturing; defect; probabilistic fatigue; El-Haddad

1. Introduction and background

Laser powder bed fusion (LPBF) is a metal additive manufacturing (AM) technology well-suited to design optimization for high value-added components [1–3]. This is possible via its piecewise methodology, summarized as the progressive layering of part cross-sections, each selectively fused from a thin powder bed spread over the previous layer, thereby generating the final part. However, LPBF is currently a costly process [1,3,4], partly due to feedstock material cost and long cycle times. As such, LPBF has thus far been limited to aerospace, high-performance automotive, biomedical, and other demanding applications which more willingly bear these costs due to their rigorous design goals, such light weighting in the face of harsh loading environments, including cyclic loading.

Whether using a safe-life or damage-tolerance approach, designing against fatigue failure requires a strong knowledge of a material's properties in fatigue. Determining and utilizing these properties is no simple task due to the stochastic nature of fatigue, exemplified by fatigue life displaying coefficients of variation typically in the range of 25-75% [5,6]. This variability is partly explained by considering the role that material and manufacturing defects play in determining fatigue life [6–8]. These principles are critical in the context of LPBF, as it is known to be plagued by semi-stochastic defect formation [9–11]. Here, the predicament of LPBF becomes clear. Ideally executed, it can achieve unique design benefits, but it is currently limited by uncertainty in quality – a disparate set of design applications and process capabilities, i.e., a lack of "fitness-for-purpose" [12].

Scatter in the fatigue properties of additively manufactured materials has been widely attributed to typically rough surface texture [13–16], high volumetric defect content [11,12,17], and microstructural imperfections and heterogeneity [18]. The former two defects both form as a result of the piecewise microscale welding process [19–21], whose efficacy relies on regular, predictable melt pool geometry. At the most basic level, surface irregularities and pores create local stress field peaks that result in crack nucleation, a phenomenon understood as cyclic shear along crystallographic slip bands, occurring rapidly at these sites. Under the circumstances of a relatively large pre-existing defect, this will progress though crack growth at microstructurally small scales, then the regime of long crack growth, i.e., stage II fatigue crack growth. In relatively defect-free wrought materials, nucleation normally makes up a significant proportion of high cycle fatigue (HCF) life [22,23]. In the case of defect-ridden materials, e.g., AM materials, it is the view of researchers that the nucleation period is vastly shortened [11,12,14,23], resulting in a commensurate overall detriment to life.

This is not to say that the details of early propagation are unimportant. Prior work has consistently shown that surface inhomogeneities [13,24] or internal pore size [23,25–27] correlate to the HCF life, for which there is a strong basis in legacy approaches to fatigue [28]. A popular framework for assessing the impact of defect severity on fatigue originates from the Kitagawa-Takahashi (K-T) diagram [29], as well as the related and popular model of El-Haddad et al. [30], which predicts the infinite fatigue limit of a material in the presence of pre-existing cracks or defects. The model references the threshold for crack growth while simultaneously bounding the predicted fatigue limit according to the defect-free fatigue limit, thus predicting the condition of either crack non-propagation or continued propagation.

These legacy models have been frequently applied to modern AM materials, with considerable success thus far. Defect-based approaches in the literature have adopted the $\sqrt{(area)}$ parameter to characterize the effective defect size and calculate the associated stress intensity factor (SIF), the parameter originally being attributed to Murakami & Endo [31], and further rigorized for AM materials by Masuo et al. [15] and Hu et al. [32]. Through a survey of available literature data, Beretta and Romano [12] showed that fatigue limits in additively manufactured Al10SiMg and Ti6Al4V were well modelled by the El-Haddad model. Further work, published by Romano et al. [27], confirmed these results for 17-4 stainless steel, as well. Beretta et al. [13] and Wu et al. [33] showed the applicability of the classical El-Haddad model to fracture initiating defects of as-built AlSi10Mg. These studies also showed that, with some exceptions, precise defect shape was not very impactful on life, due to defects quickly transiting to a lower SIF elliptically-shaped crack form, affirming the effective size approach. Defect size and location have been found to be found to be largely responsible for immense scatter in fatigue life [12,17,25,32,33].

The classical, or infinite life El-Haddad model is limited in that it only predicts infinite endurance or eventual failure but not life at failure. Ciavarella and Monno [34] offered an adaptation to address this, which incorporated both stress-life (S-N) and fatigue crack growth (FCG) models to predict finite life. Further application of these concepts to AM materials was performed by Sheridan [35], who was able to generalize the finite life model to predict finite life at varying loading ratios. These efforts represent preliminary investigations into finite life estimation, and further work is needed. Notably, research efforts are still testing the accuracy of various FCG models for AM materials [14,25,36,37], which might be used to construct updated finite life El-Haddad models.

A limited number of in-depth examinations of the ‘killer’ defects which initiated fatigue failure in AM alloys have been conducted to help bolster the understanding of these phenomena. Studies of LPBF manufactured Inconel 718 [38], 17-4 stainless steel [27], and Ti-6Al-4V [32] have all successfully correlated initiating defect size to life, post-mortem. In these works the authors assumed that materials of same pedigree, i.e., same LPBF processing parameters, feedstock material, post-processing history, etc. were well described by representative X-ray computed tomography (XCT) scans which characterized their porosity. Under this assumption, the statistical processing of porosity data shown in Ref. [25,26,33,39,40] with fatigue models such as the finite life El-Haddad adaptation could enable fatigue life predictions with minimal destructive testing necessary.

Critically, many fatigue and fracture studies of AM materials have taken a somewhat narrow approach to defining the processing parameters that control material pedigree. Typically, feedstock powder quality, laser processing parameters (e.g., power, speed, spot size), build strategy (e.g., scan pattern, layer height, specimen orientation to the build direction), heat treatment, and post processing (e.g., machining, finishing) have been considered to drive the process-structure-properties chain. Despite this, recent work [41,42] has shown significant mechanical property variability within a single ‘lot’ of LPBF material, i.e., a build(s) utilizing the same LPBF processing parameters. Prior work is limited in the context of fatigue, but Soltani-Tehrani et al. [43] and Li et al. [42] demonstrated the dependence of fatigue life on specimen location within the build volume. Further investigation is required, but these findings may be a result of porosity caused by redistribution of spatter particles onto the powder bed and attenuation of the laser beam by condensate clouds.

Increasingly, researchers acknowledge how the poor process repeatability of LPBF leads to varying defect content and therefore varied mechanical performance. It may be that these are unavoidable signatures of the LPBF process, and in that case, robust statistical characterization and fatigue prediction approaches must be developed. In the present work, a large fatigue data set (n = 45) was leveraged to reveal that nominally identical components within and across builds displayed both low-defect-quantity/long-life and high-defect-quantity/low-life tendencies associated with specimen location. This scatter was characterized probabilistically and mechanistically, through safe-life and damage-tolerant approaches respectively, in an effort to advance tools such as the finite life El-Haddad model or probabilistic predictors which can account for manufacturing defects. Critically, this approach simulated industrial applications by using optimized processing parameters, virgin powder, densely populated build volumes (i.e., high efficiency production), and multiple builds (i.e., high quantity production) which demonstrated the need to consider build volume location as a relevant process parameter which controls defect content and fatigue life.

2. Material and methods

2.1. Specimen manufacture

All specimens were manufactured using a commercial *EOS M290* LPBF system. Four identical builds were carried out, numbered A1, A2, A3, and A4. Each build included 12 specimens intended for fatigue testing, 10 for tensile testing, and 3 witness coupons for microstructural analysis. The results of tensile testing can be found in prior work [44]. The layout of the builds, all built on 250 x 250 mm medium carbon steel build plates, can be seen in Figure 1. The as-built geometry of the fatigue and tensile specimens was identical, shown as a 91 mm long hexagonal prism in Figure 1, longitudinal axes perpendicular to the build (+Z) direction, i.e., horiztonal. Specimens were identified by their unique number, e.g., 2-5-A1, which specifies their location, e.g., row 2, 5th position from left, and the build number, e.g., build A1. It should be noted that three specimens from build A1, 3-1, 4-2, and 5-1, were not available for fatigue testing due their improper manufacture. These specimens, and one tensile specimen with similar issues, are marked with asterisks on Figure 1. Specimens were manufactured according to best practices for exposure order, i.e., the sequence within a build layer that specimen slices are fused in. This practice aimed to fuse specimens furthest in the direction of gas flow and recoat first. The numbers in parentheses in Figure 1 represent exposure order.

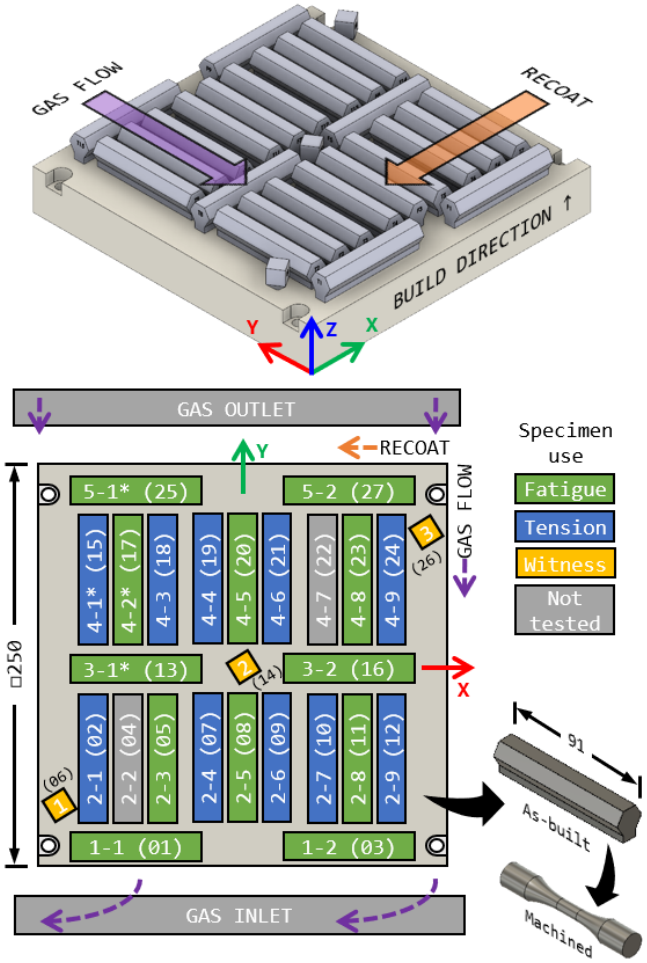

Figure 1. Layout of mechanical test specimens and witness specimens on a 250 mm square build plate, used for all four builds. Specimens are numbered and their exposure order shown in parentheses. Asterisks (*) mark build A1 specimens which were not properly manufactured. Shielding gas flow is shown schematically by dashed purple arrows.

All specimens were manufactured using 17-4 stainless steel powder feedstock, never recycled. This precipitation hardening alloy, also called 17-4 PH, is common in industrial and research contexts due to its mix of affordability, strength, fatigue performance, and high heat/corrosion resistance. It is readily available in powder form from commercial suppliers and studied in the recent literature. All powder used was from a single lot acquired from *Praxair Surface Technologies*¸ under the commercial product name of *Truform 174-161*. The powder was manufactured via gas atomization and had a powder size distribution (PSD) specified by the manufacturer to have the following 10th, 50th, and 90th percentiles in diameter distribution, measured in accordance with ASTM B822-20: d_{10} = 25, d_{50} = 37, and d_{90} = 55 µm. The manufacturer also reported 1% and 0% of particles to be above 53 and 63 µm, respectively, measured in accordance with ASTM B214-16, and a tap density of 4.57 g/cm^3, measured in accordance with ASTM B527-20. Powder chemistry was also reported, and for reference, met all chemistry specifications of UNS S17400, as per ASTM A693-16.

All specimens were manufactured using the same nominal LPBF processing parameters, provided by the machine manufacturer, detailed in Table 1. Specimens were built using a ‘stripes’ scan strategy, which alternated the orientation of a raster-based stripe (12 mm width) scan pattern by 67° between each layer. The time between the start of each sequential layer was held to a constant. After manufacture via LPBF, all specimens were heat treated in the same lot in a vacuum furnace in their as-built condition on their respective build plates. Specimens were solutionized and aged to the H1025 condition, according to AMS 2759/3, via solutionizing at 1038 °C [1900 °F], quenching in a backfilled Ar gas atmosphere to below 32

°C [90 °F], and aging at 552 °C [1025 °F] for 4 hours. After heat treat, specimens were removed from the build plate by band sawing (see Figure 2). As well-evidenced by prior work [9,16,36], the solutionizing step accomplished both stress relief and microstructure homogenization.

Table 1. LPBF build parameters

Parameter	Value
Layer height	40 µm
Laser power	220 W
Scan speed	755 mm/s
Hatch spacing	110 µm
Beam spot diameter (approx.)	80 µm
Build plate temperature	80 °C

As-built specimens were hexagonal prisms, nominally 15.20 mm across flats and 91.00 mm long, shown in Figure 2. After LPBF manufacture, heat treat, and removal from the build plate, specimens were machined on an CNC turning center to their final geometry, also shown in Figure 2. The fatigue specimen design was adherent to design guidelines of ASTM E466-15, and had a gage section nominally 6.00 mm in diameter. After machining, fatigue specimens were polished up to P2000 grit to remove all tool marks and accomplish a lay parallel to the direction of applied stress. Surface roughness, measured as R_a, was found to be on average 0.023 µm, measured by extracting a profile parallel to the specimen axis from the unfiltered areal data attained from a *Zygo ZeGage* coherence scanning interferometer. This value met the recommendations of ASTM E466-15. No specimens showed surface defects visible to the eye. The -X facing end of specimens 1-2 and 3-2 were turned down to 4.00 mm in diameter (see Figure 2), to prepare these sections for further analysis via XCT.

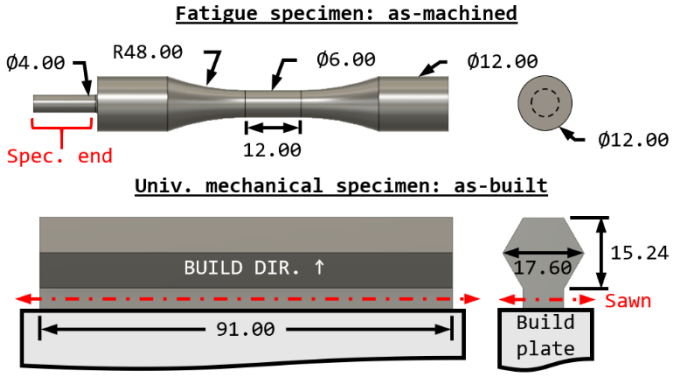

Figure 2. Fatigue specimen machined geometry as-built (bottom) and as-machined (top). All units are in mm.

2.2. *Fatigue testing*

Fatigue specimens were tested with an *MTS* 98 kN capacity servo-hydraulic universal testing machine. An *Interface* 111 kN capacity in-line load cell was used for force data acquisition. A total of 45 force-controlled fatigue tests were conducted; 9 on A1 specimens and 12 each on A2, A3, and A4 specimens (see Figure 1). All fatigue specimens were tested using an 8 Hz sinusoidal forcing wave, a loading ratio of R = 0.1, and a maximum stress σ_{max} = 867 MPa. For reference, this stress level was 76% of the average yield stress, σ_y = 1146 MPa, seen in a sample of identically manufactured specimens [44]. Loading was selected based on initial tests with representative specimens to produce failure in the high cycle fatigue (HCF) range. Force data was periodically monitored for error from the commanded level and showed no aberrations.

2.3. *Porosity assessment via XCT*

After fatigue testing, several specimens of interest were further analyzed by XCT to assess their volumetric defect content. All specimens from locations 1-2 and 3-2, four specimens per location corresponding to the four builds, were inspected as shown in Figure 3. Only a representative volume from the specimen -X facing end, previously machined to 4.00 mm in diameter was scanned. This limited X-ray attenuation and thus enabled an acceptable voxel size (11 µm) to be achieved. Note that these specimen

ends were never under stress during prior testing and are considered representative of the specimen gage volume due their relatively near location compared to the length scale of the build volume (250 mm).

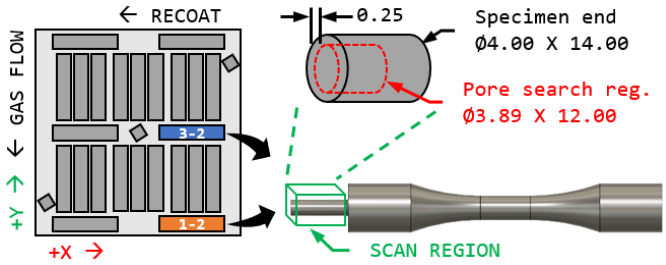

Figure 3. Selected specimen locations for XCT (left). CT scanning region of specimen end (right-bottom). Porosity search region within scan region (right-top). All units are in mm.

The selected specimens were inspected with a *Zeiss Metrotom 800* industrial XCT system. Scanning parameters, summarized in Table 2, were selected to maximize the contrast between the specimen and background while striving for the minimum achievable voxel size. Volumetric reconstruction was completed using the native machine software (*Zeiss Metrotom OS*) which utilized a Feldkamp-David-Kress reconstruction algorithm and a Shepp-Logan digital filter. Further data analysis was performed using the commercially available software package, *VGSTUDIO MAX 3.4*. Surface determinations were conducted using a gray-value gradient maximization technique capable of sub-voxel interpolation. This method referenced an initial surface threshold, based on a 50% isovalue, and searched for a gray-value gradient maximization over a four-voxel range centered on and normal to the initial threshold. The software's integrated porosity determination tools were used to identify pore volume, size, shape, and location. The search algorithm parameters were tuned on a representative specimen to capture a large proportion of pores and produce a low false positive rate, as judged by a visual inspection of scan slices. Only pores with a volume of 22 voxels (29,282 μm^3) or greater were considered, as this size was correlated to visually identifiable pores in scan slices. This search routine was replicated on all scanned specimens in a cylindrical region that was 3.89 mm in diameter, 12.00 mm long, and 0.25 mm offset from the specimen end, as shown in Figure 3. Being offset from the specimen surfaces, major artifacts due to beam hardening and cone beam effects were not considered in the porosity analyses.

Table 2. XCT scanning parameters

Parameter	*Value*
Voxel size	11 µm
Focal spot size	8 µm
Voltage	130 kV
Current	61 µA
No. projections	1200
Physical filter	0.25 mm, Cu

Due to their complex morphology, the subsequent analyses quantify pore size according to their equivalent spherical diameter, in units of [µm]. This parameter is simply the diameter of a sphere whose volume is equivalent to the volume of the pore. Ref. [42] utilized a similar approach. This measure is insensitive to local pore boundary surface determination errors.

2.4. Quantitative fractography

Because force-controlled fatigue testing was conducted, specimen failure constituted complete net section fracture. Specimen fracture surfaces were inspected on *Zeiss Ultra 60* SEM, using acceleration voltages that ranged from 10 to 20 keV, a working distance of approximately 10 mm, and signal mixing from both the primary and secondary detectors. Fracture surfaces were cleaned with a light amount of compressed air prior to inspection, but otherwise not altered. Quantitative fractography analyses were conducted to assessing the size, location, and nature of the fracture initiating defect. The standardized methodology for AM material defect size determination set out by Masuo et al. [15], which is similar to that used in Ref. [32] and based on the commonly used methods of Murakami and Endo [31], was applied to determine the effective area of a defect, $area_{eff}$, and categorize a defect as sub-surface or internal. The

effective size of a defect was then quantified as $a_{eff} = \sqrt{(area_{eff})}$. The referenced procedures [15] may be briefly summarized as follows:

1. The effective area of a defect is the approximately elliptically shaped convex hull which subtends its extremities. For sub-surface defects, this hull includes the ligament which separates the outer edge of the defect from the surface.
2. A defect is classified as sub-surface if:
    a. It intersects or is tangent to the surface.
    b. The width of the ligament which separates the edge of the defect nearest the surface from the surface is smaller than the width of the defect.
3. If two defects are near to each other, and the width of the ligament which separates them is less than the width of the smaller defect, the convex hull which defines the effective area includes both defects.

Defect area was characterized using above procedures, the SEM micrograph scale bar, and the *Fiji* distribution of the open-source image analysis software *ImageJ*. Hereon, the $a_{eff} = \sqrt{(area_{eff})}$ parameter is used to describe the defect size and is simply referred to as "defect size" in the text.

3. Results

3.1. Fatigue life variation and trends

The results of the force-controlled fatigue tests, all under the same loading conditions, are shown in Figure 4 where fatigue life is shown on a logarithmic horizontal axis and specimens are grouped according to their originating build plate locations, shown on the vertical axis. The originating build, i.e., A1, A2, A3, A4, did not appear to introduce any preference for low- or long-life, as evidenced by the lack of any systematic patterns in life respective to each specimen build number. Prior work on a related data set also showed no statistically significant differences between the distributions of life respective to each build [44].

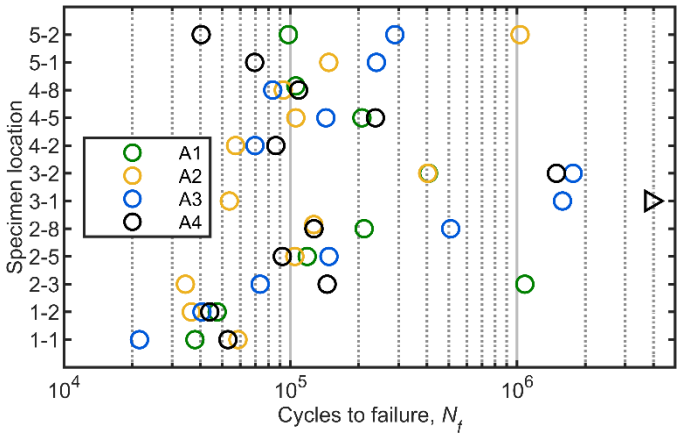

Figure 4. Fatigue life under identical loading conditions, organized by specimen location. Run-out is signified by a right-pointing triangle.

Considering the entire data set, fatigue life showed a high degree of scatter. The minimum number of cycles to failure displayed was $N_f = 21{,}546$ cycles (specimen 1-1-A3), and the maximum was $N_f = 1{,}766{,}801$ cycles (specimen 3-2-A3). One specimen, 3-1-A4, was run-out, with testing terminated at $N = 3{,}900{,}000$ cycles prior to failure. This specimen's behavior is further examined in section 4.1. The coefficient of variation seen in life, defined as $s_{Nf}/\overline{N_f}$, where s_{Nf} is the standard deviation of the data and $\overline{N_f}$ is the mean of the data, was 194%. This is an exceptionally high level of variation, when compared to HCF in conventionally manufactured structural alloys, or even some prior results reported for LPBF processed alloys, which have generally sampled less dense or more local build volumes.

In addition to the overall scatter being of note, further observations can be made by referencing Figure 5 for the mean life and variation in life attributed to each specimen location. Certain locations appear to

display uncharacteristically low life (e.g., 1-1, 1-2) with relatively low scatter, while others display intermediate life with varying degrees of scatter, and still others display high life with considerable scatter (e.g., 3-1, 3-2). Figure 5 shows that the data displays definitive heteroscedasticity, i.e., the variation in life appears to be a function of mean life. This would suggest that an intrinsic property of the specimen which drives fatigue life, such as porosity content, varies with location within the LPBF system build volume. Note that data set sizes are relatively small, 4 specimens for most locations and 3 for locations 3-1, 4-2, and 5-1. Due to this, the trend seen in Figure 5 may be subject to some levels of uncertainty. Considering the standard deviation of the logarithm of life data did not eliminate this trend.

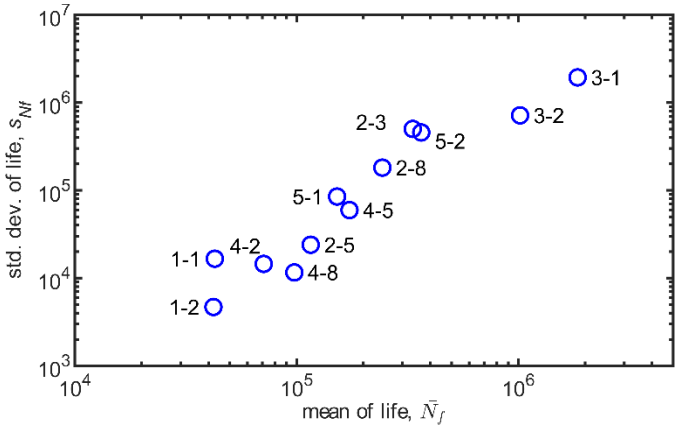

Figure 5. Fatigue lives mean and standard deviation associated with each specimen location.

3.2. Fracture initiating defect types and trends

All failed fatigue specimens were inspected to discern the important features of their fracture surfaces. Figure 6(a-b) shows the macro-scale fracture surface topography of specimen 1-1-A1, representative of most specimens and typical of fatigue failure in an axially stressed a ductile metal. The topography shown was attained via a *Keyence VR-5000* high resolution structured light scanner and analyzed with the native instrument software. A fracture growth region is apparent, clamshell in shape, adjacent to the specimen surface, and oriented normal to direction of stress. A crack, originating in the subsurface region, progressed through this region due to cyclic loading in a brittle manner until it was of a size that sufficiently reduced the stress bearing area of the specimen. This led to final failure via semi-ductile fast fracture in the remaining net section of the specimen. Ductile dimples were discerned at high magnifications in areas outside of the stage II growth region. Shear lips, oriented approximately 45° from the stress axis, also formed during final failure. Minor plastic deformation was noticeable on the free surfaces of the specimen close to the shear lips. Nearly all specimens exhibited a similar macro-scale features in their fracture surfaces, albeit with some differences in the form of the shear lips.

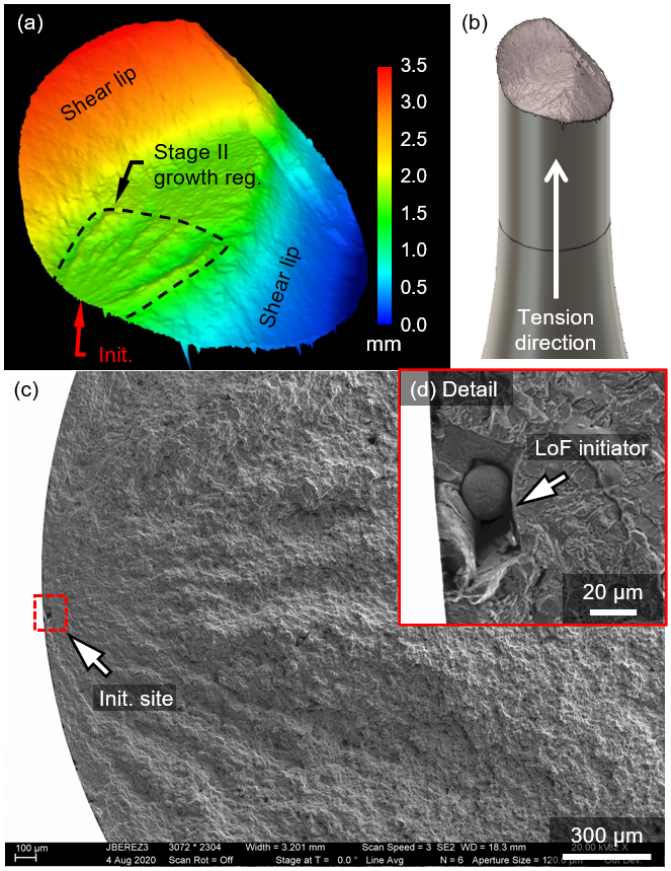

Figure 6. (a-b) Typical fracture surface topography. (c-d) Fatigue crack growth region and fracture initiating defect.

Figure 6(c-d) shows the features of a representative fracture growth region and the identification of the initiating defect. The growth region displays prominent chevrons, seen in Figure 6(c), which clearly identify an initiation site near the specimen surface. The inset, Figure 6(d), shows the initiating defect in detail, which was a lack-of-fusion (LoF) pore, approximately 80 µm in its largest apparent dimension. Due to the brittle fracture mechanism, defect shape was likely well preserved. Using analogous methods of initiation site identification, defect type categorization (further expanded upon in this section), and standardized size/location determination methods (refer to Section 2.4), all 44 failed specimens were analyzed. Results are tabulated in Table 3, which groups specimens in four life span regions; low-, intermediate-, long-, and very long-life.

Table 3. Fractography observations

Life span	**Low-life** 20,000-60,000	**Intermediate-life** 60,001-100,000	**Long-life** 100,001-400,000	**Very long-life** 400,001-2,000,000
No. of specimens (% of total)	12 (27%)	8 (18%)	16 (36%)	8 (18%)
Init. defect details		*Observation freq.*		
>1 growth regions	1	0	0	0
Interior init. site	0	0	0	2
LoF defect type	11	7	13	6
Other defect type	0	1x inclusion	2x gas pore	1x gas pore
Uncategorized type	1	0	1	1
Intergranular features	8	0	1	1
Defect size range, a_{eff} [µm]		*Observation freq.*		
15-25	0	0	0	1
25-50	0	2	14	4
50-75	2	5	2	0
75-100	4	0	0	0
100-125	4	1	0	1
125-200	1	0	0	0
150-200	1	0	0	2

Examining the table for trends in the initiating defect type shows that LoF defects initiated the vast majority (38 of 44) of failures in life spans. Overall, small microstructural features, such as inclusions, precipitates, or micro cracks generally did not appear to initiate fracture. Three were likely gas pores, identified by their small size (<30 μm) and circular form, seen in the long- and very long-life spans, and exemplified by Figure 7(a). The majority of LoF defects were generally identified by their torturous form and cellular surface texture, exemplified by Figure 7(b-d). The defect interior surfaces show grain boundaries between mostly equiaxed cells, and the martensite morphology within a cell is even visible, best seen in Figure 7(d). A small number of LoF defects did not display such features, but instead showed what appears to be an oxidized surface, as in Figure 7(e-f). Some features of solidification of a free surface, such as micro-ripples, are also displayed, best seen in Figure 7(f). These features were also seen in some fractographs of defects with cellular textures, confirming that they indicate a LoF pore. The small number of "uncategorized" initiating defects were either difficult to observe in detail or did not display features that could be used to definitively categorize them.

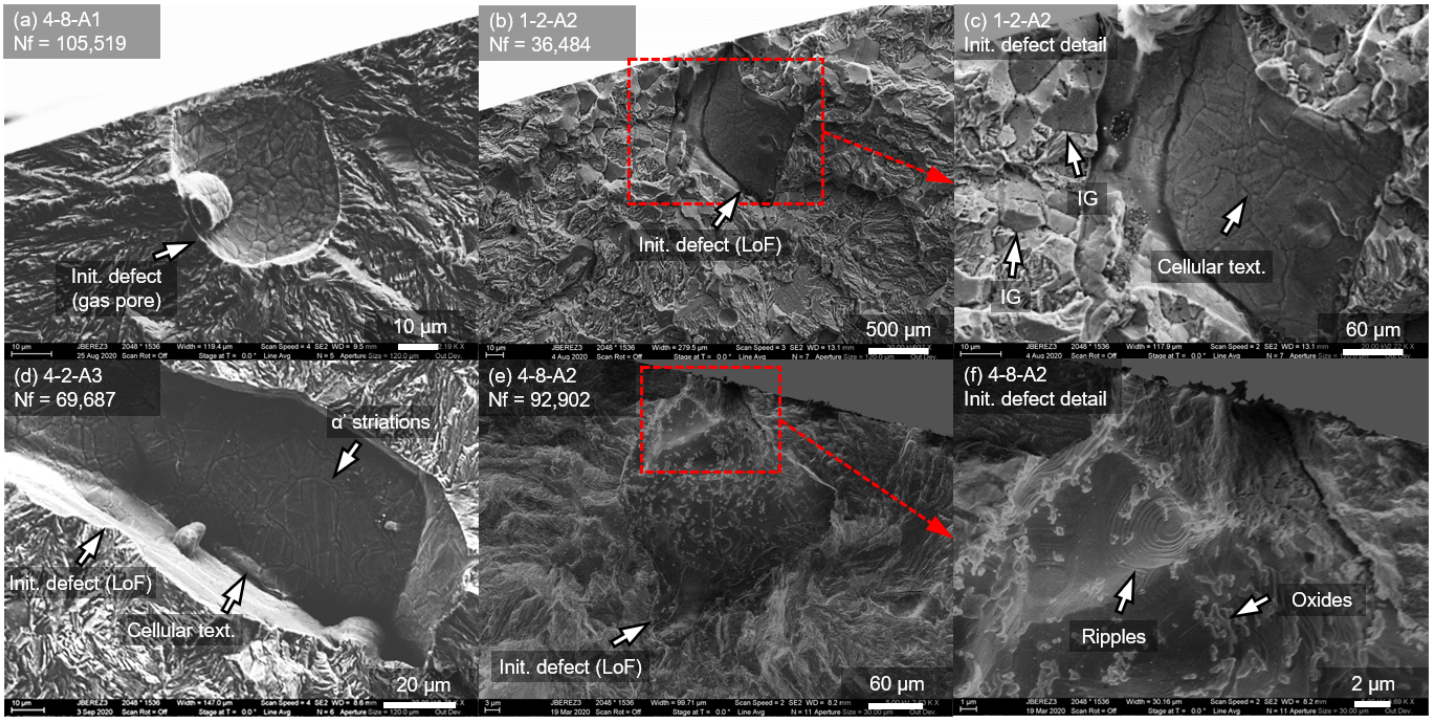

Figure 7. Selection of distinguishing fracture initiator features.

Nearly all specimens (42 of 44) had initiation sites in the sub-surface region of the specimen. Only one specimen had more than one apparent initiation site, low-life specimen 1-1-A4. These outliers are more closely examined in section 4.5. One other classification shows a notable trend – a large proportion of low-life specimens displayed intergranular (IG) fracture features surrounding the initiating defect, exemplified by Figure 7(c). Commonly, IG or decohesive rupture observations are related to causes such as stress corrosion cracking, embrittlement, or intergranular segregation of weak low melting temperature elements. These explanations do not fit the exhibited results, as testing environment and solidification microstructures should not differ between these specimens and others. More likely, the high local stress magnitudes created by the large defects in these low-life specimens played a role in early growth via IG mechanisms. Supporting this, at high magnifications, the IG sites show signs of dimpled IG fracture, which may have originated from the partially incohesive precipitates of the overaged H1025 alloy condition.

Figure 8 shows that the SIF range associated with each initiating defect on the vertical and life on the horizontal. SIF was calculated as $\Delta K = Y\Delta\sigma\sqrt{\pi a_{eff}}$, where Y = 0.65 and 0.5 for sub-surface and interior

defects, respectively. As such, for a constant $\Delta\sigma$, ΔK scales with a_{eff}, barring variations in Y. When both quantities are logarithmically transformed, they appear to trend linearly over a limited range, albeit with some scatter – as expected, larger defects which drive larger SIF values are associated with lower life. This dominant trend has been approximated with the "low, intermediate, & long-life" short-long dashed black trend line. Notably, most observations beyond approximately N_f = 200,000 depart somewhat from this trend. A grouping of data, contained in the "long & very long-life" dashed blue boxed, shows this behavior. This is partially explained by the effect of near-threshold crack growth behavior, as these data show ΔK values near the threshold SIF, ΔK_{th}, represented by the gray dashed horizontal. As such, FCG rates may be much lower for a portion of these specimen's lives, possibly indicating a non-negligible nucleation or short crack growth stage. Behavior in this stage would not necessarily be captured by ΔK, and thus does not trend with the rest of the data on the plot. It should be noted that ΔK_{th} was drawn from Ref. [27] for the relevant material, heat treatment, and loading ratio. Additionally, several observations in the long-life regime, specimens 2-4-A1 and 3-1-A3, exhibited life over 1,000,000 cycles despite their large defect sizes over 100 µm. This is partially explained by these defects being located in the interior of the specimen, a concept discussed in further detail in Section 4.5. Specimen 5-2-A2, a sub-surface defect, showed similar behavior without a clear explanation.

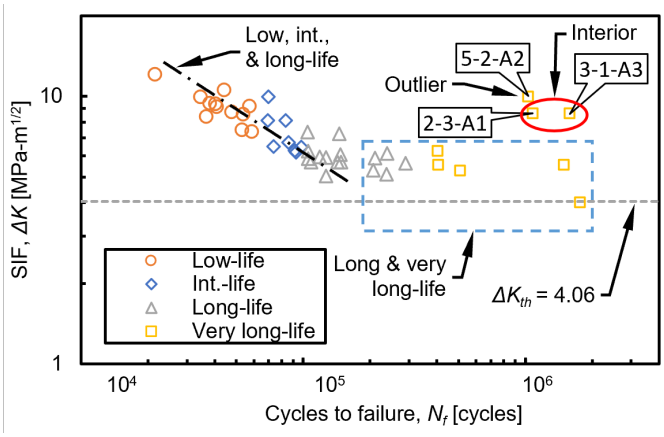

Figure 8. SIF associated with init. defect, vs. exhibited life.

3.3. Porosity content associated with specimen location

Porosity visualizations of the sampling regions from specimens 1-2-A1 and 3-2-A1, which are representative of their respective specimen locations, are shown in Figure 9(a-b). XCT has been well established as a strong method for characterizing volumetric defect content and crack growth [37,45]. The results of an automated porosity analysis are shown; pores are highlighted and colored according to their equivalent spherical diameter. Note that pores are plotted as simple spheres on their centroid positions, with their diameter scaled by a constant factor to improve legibility. Specimen 1-2-A1 contained more pores (n_{tot} = 254) and larger ones, whereas specimen 3-2-A1 had fewer (n_{tot} = 46) and smaller pores; most less than 50 µm in size. Two of the largest identified pores in 1-2-A1 are shown in Figure 9(c-d), which are cross sections of the reconstructed volume. Both pores were approximately 200 µm in their largest apparent dimension, and complex in their morphology. Both appear to contain small circular features, identified by arrows in the figure, where are on the order of typical powder size range (d_{10} = 25 µm, d_{90} = 90 µm), providing further evidence large LoF pores.

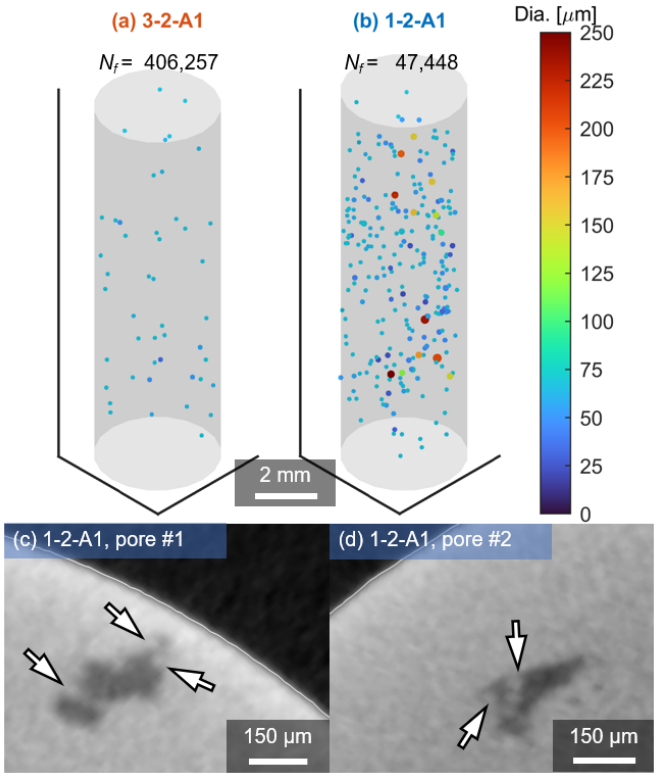

Figure 9. Porosity visualizations of specimens (a) 3-2-A1 and (b) 1-2-A1. Pores are colored according to their equivalent spherical diameter. Pores are plotted as simple spheres and their size has been scaled for legibility. (c-d) Reconstructed XCT volume cross-sections of specimen 1-2-A1, showing the two largest identified pores.

An identical automated porosity analysis was executed on all scanned specimens, corresponding to the four specimens each from locations 1-2 and 3-2. Figure 10(a) shows the results in the form of a boxplot, with the noted percentile demarcations. The total number of pores, n_{tot}, is also shown for each specimen. The volumes from location 1-2 had a total number of pores in the range of 226-363, while those from location 3-2 had 26-46 pores. In most cases, the 97th percentile of pore diameter present in 3-2 locations, on the order of 75 µm, was approximately equivalent to the 75th percentile seen in 1-2 locations. The 75th-97th percentile ranges for the 1-2 locations were quite large and ranged from approximately 53-150 µm. Three of four scanned volumes from location 1-2 had a small number of very large pores ranging from 150-250 µm. Figure 10(b) more clearly represents the difference in the total quantity of pores seen in the investigated volumes, as directly implied by the area of each histogram. Here, the data sets respective to the four specimens from each location have been combined to form an aggregate data set for each location.

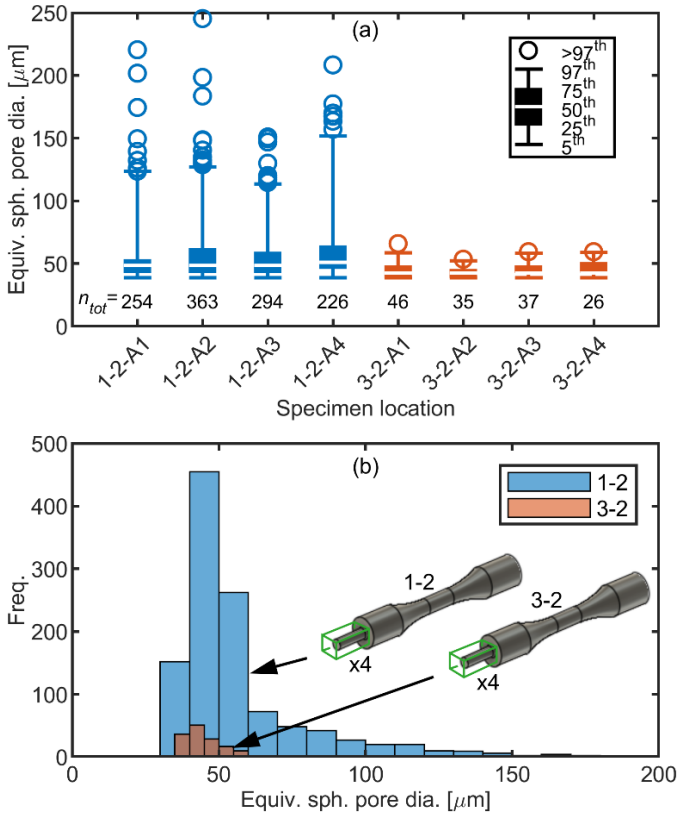

Figure 10. Porosity size data determined form XCT scans. (a) Box plots of pore equivalent spherical diameter respective to each scanned specimen. (b) Histograms of pore equivalent spherical diameter respective to each specimen location.

4. Discussion

4.1. Life dependence on specimen location

Figure 11 provides the mean fatigue life associated with each specimen location. Run-out data was not included in this calculation. Correlating specimen locations 1-2 (average life = 42,000) and 3-2 (average life = 1,017,000) to the porosity analyses in Section 3.3 clearly associates porosity distributions with larger and more frequent pores to lower fatigue life, and vice versa. In fact, both the mean and variation in life respective to specimen location were driven by the nature of how a specimen gage section sub-surface region statistically samples the overall local porosity content. The sample of a high porosity content region, which the volumes specimens from location 1-2 represent, was more likely to contain a large pore from the distribution tail. Thus, these specimens were likely to contain a 'killer' pore of similar size (low-scatter) and large size (low-life). This was less likely for specimens which originated from low porosity content region, thereby producing high-scatter and long-life. This would also explain the run-out of specimen 3-1-A4, assuming a low defect content similar to the 3-1 location. Extreme value statistics of a defect population related to the stressed volume have been used to explain these trends [25,33,39].

Using average life as an indicator of high defect content, Figure 11 indicates the -Y region of the build volume, i.e., the gas flow downstream region, as high in defect content. Here, specimens 1-1 and 1-2 have a characteristically low life, around 40,000 cycles. Further trends are not readily apparent, other than that the center of the build region showed very long life, on average. Specimens 3-1 and 3-2 both showed average lives above 800,000 cycles.

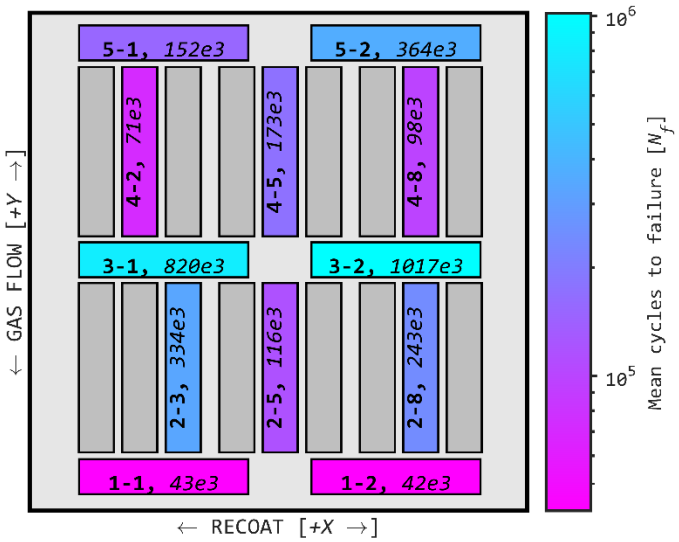

Figure 11. Mean life of tested specimens associated with their location.

The defects which populate the downstream region are hypothesized to have been caused by a combination of effects from laser welding process byproducts such as condensate and spatter which were not sufficiently removed from the build volume. Condensate forms from the metal vapor cloud present over the melt pool. This cloud, when sufficiently exposed to the laser, forms metal condensate, which is small particles, on the scale of tens of nm [46,47]. Spatter can be generalized as solid or liquid particles ejected from the melt pool [46,48,49]. Metallic jet spatter particles, specifically, have been reported as ranging from similar in size to the feedstock powder particles [46,47] approximately 2-4 times larger [47,49,50], and often compositionally impure [47,48,50,51]. During ejection, the particle may join with solid powder particles near the melt pool boundary or with other liquid particles ejected forming large, agglomerated spatter particles. Constantly flowing shielding gas is used in LPBF machines to evacuate both condensate and spatter from the build region.

The study of condensate and spatter effects is limited, but several investigations support the findings of this work. Condensate clouds, if not sufficiently removed from the process area by the flowing shielding gas, can attenuate the laser beam before it reaches the powder bed, resulting in an imparted power loss reported to be as high as 40% [52] and thus potentially smaller melt pools and LoF between laser paths and layers. Spatter has been identified on as-built surfaces in areas of poor gas flow by multiple authors [53,54], which appear to generally be in the downstream region [52,55]. Spatter may not be effectively evacuated by low-velocity and turbulent gas flow [52,55], which would be the case in the present work. Large spatter particles could create local instabilities in the melt pool and lead to poor local power packing.

As shown in Figure 1, the gas flow in the LPBF machine is severely redirected into the outlet nozzle over the -Y build region, possibly leading to lower velocities and less laminar flow in this region. Low-life specimen locations 1-1 and 1-2 are in this region. Overall, the large LoF defects shown in the XCT and fractography analyses of these specimens can likely be attributed to a combination of spatter and condensate effects. Notably, a densely populated build volume, such as in this work, can be assumed to produce a proportionally large amount of process byproducts. The effects on end-component quality are not fully understood, but a limited number of works show greater porosity in both downstream [52] and upstream [56] regions with potential detriments to ultimate strength [57]. Soltani-Tehrani et al. [43] and Li et al. [42] both theorized that byproducts produced porosity and a location-based dependence in fatigue life, but these works might not have revealed the full scope of variability.

4.2. Fatigue life heteroscedasticity

The noted trends in fatigue life seen in Figure 5 and described Section 3.1 can be summarized as heteroscedastic in nature. Conventionally, heteroscedasticity in fatigue refers to different levels of scatter

correlating to different stress or strain levels, approximated by the life distributions in different shades of green in Figure 12. A strong example can be found in Ref. [58]. It should be noted that experimental data is generally not normally distributed, and the figure only illustrates approximate behavior. While deterministic predictors of life or crack growth, such as stress-life curve, strain-life, or long-crack FCG models are often used to model fatigue behavior, they primarily serve as a best-fit model, such as the black stress-life curve in Figure 12. It is important to recognize that there is a significant scatter band, based on the variation displayed at each stress level, which better summarizes fatigue behavior, such as the red short-long dashed 95% confidence interval bounds.

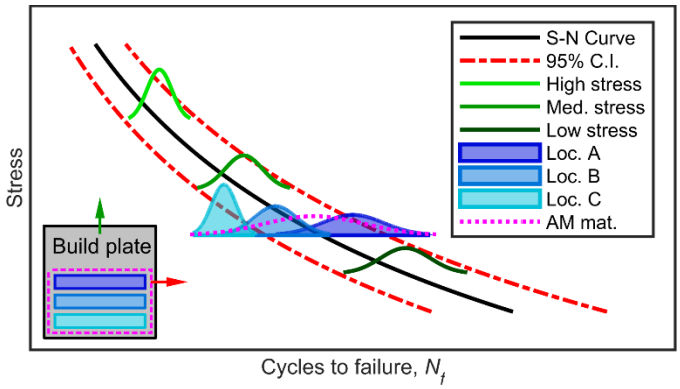

Figure 12. Heteroscedasticity in fatigue. Green curves show typical behavior, shaded blue curves show observed behavior. Distributions and build plate locations are approximations.

The data examined in this work are subject to an added dimension of heteroscedasticity different than what is typically observed in fatigue. Long-life specimens still showed high scatter, but applied stress was constant. Specimen location within the LPBF system build volume can be considered an added independent variable, as approximated by the blue shaded life distributions in Figure 12. As will be expanded upon, these locations contain different defect populations, which drive distinct S-N behavior. Despite this, as a single material lot, the overall scatter is still of concern, approximated by the magenta distribution in Figure 12. Critically, current qualification approaches in LPBF do not typically systematically sample build plate locations, meaning that the full scope of variability may not be captured. In an extreme scenario, a location with favorable fatigue properties, such as the dark blue "location A," may be used to establish design allowables, which thus fail to capture the behavior of parts built in locations B or C in a production run.

4.3. Describing fatigue life probabilistically

Thus far, fatigue life has been presented in a framework which implies that a unique specimen location produces a unique characteristic life distribution. Nonetheless, current practices in the broader metal AM community do not generally emphasize specimen location as a LPBF process variable, instead considering these specimens to be of a single material lot. In keeping with these practices, it is worthwhile to ask if the overall fatigue life distribution exhibited in this work can be summarized as a single variable.

To accomplish this, the entire fatigue life data set (44 data points) was treated as a random variable. Several parametric probability distribution functions (PDFs) of interest were then fitted to the data using the maximum likelihood estimation (MLE) method [60,61]. These were the lognormal and Weibull distributions, which historically have been used to model fatigue data [62–64], as well as numerous other 'weak-link' governed phenomena, such as those studied in the reliability modeling field [65]. Both PDFs are capable of being highly right-skewed, which accurately represented fatigue life as having relatively infrequent long-life behavior. The fitted distribution parameters, and their associated 95% confidence intervals, are provided in Table 4.

Table 4. Parametric distirbution parameters

Parameters	**Upper C.B.**	**Parameter value**	**Lower C.B.**
	Lognormal		
μ (mean)	11.4577	11.7921	12.1264

σ (std. dev.)	0.9087	1.0872	1.3935
	Weibull		
η (scale)	1.6146×10^5	2.3733×10^5	3.4886×10^5
β (shape)	0.6637	0.8171	1.0059

To evaluate the fitness of these distributions to model the data, they have been plotted along with the experimental data in Figure 13(a). Here, life data, shown on a logarithmic horizontal axis, is presented in terms of the empirical survival function, also known as the Kaplan-Meier estimator, where the probability of survival past N cycles is shown on the vertical axis. Confidence bounds were calculated using Greenwood's formula. An example on applying these methods in detail can be found in Ref. [44]. The parametric models are plotted as survival functions, which is merely the complement of their continuous cumulative distribution functions (CDF). Through these tools, a safe-life approach can be taken, which uses descriptive distributions to estimate lower-bound performance thresholds, such as 99% or 95% survival probability. Other authors [58,59] have expanded these concepts to the entire S-N curve.

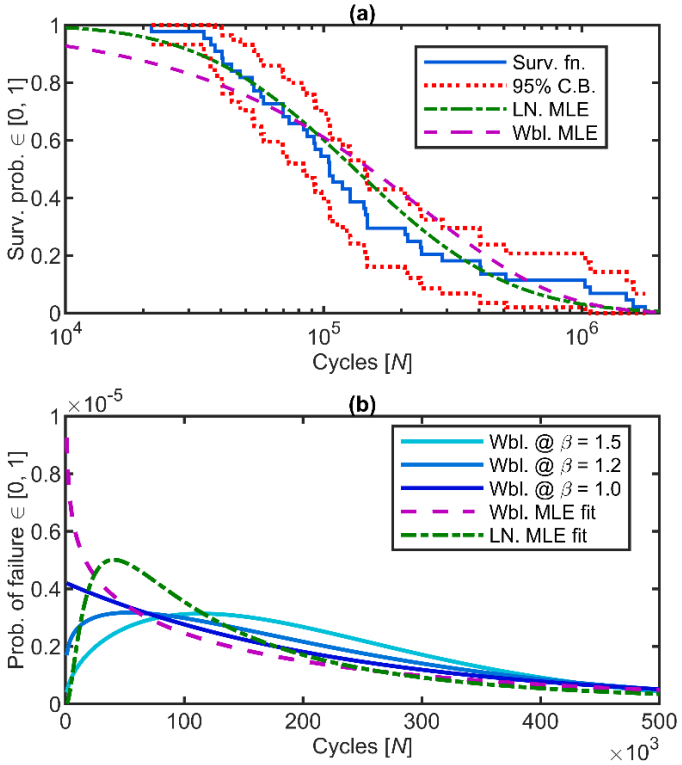

Figure 13. (a) Empirical survival function and confidence bounds as well as fit lognormal (L.N.) and Weibull (Wbl.) distirbution survival functions. (b) Fit lognormal and Weibull PDFs, including several Weibull distributions with altered shape parameters.

By assessing Figure 13(a), the lognormal function was determined to provide a better model of the data. It is almost fully contained within the empirical survival function confidence bounds and provides a fairly accurate model throughout the range of life. It slightly underestimates survivability at low-life, which is conservative but not overly so, thus marking this model as a potentially useful tool for reliability modeling and design. The Weibull model is a far poorer fit throughout the span of life, and vastly underestimates survivability at low life, making it overly conservative. For further insight Figure 13(b) is provided, which shows models' normalized PDFs on a linear scale of life. The fit lognormal distribution, which is mathematically constrained to always be a highly skewed bell shape, tapers off in value at zero life. On the other hand, the fit Weibull model is exponential in shape, which leads to very high probability of failure at zero life, and hence it's overly conservative nature. It should be noted that while the standard Weibull function is used here, the three-parameter Weibull function was also tested, with the shift value set to different values approaching the lowest exhibited lives. The observed fits and trends were analogous.

The poor fit of the Weibull model is understood via the additional curves shown in Figure 13(b), which show the distribution with the fit η value, but varying shape parameter values (β = 1.0, 1.2, 1.5). Exponential shapes ($\beta < 1.0$) do not represent the physical phenomenon, but the bell shapes ($\beta > 1.0$) are mathematically limited in skewness and is also inaccurate. As it stands, the historically popular Weibull may not be well suited to modeling the highly defect ridden LPBF material studied here.

4.4. Defect-based fatigue life prediction

In order to construct a deterministic predictor of specimen finite life, the generalized El-Haddad model developed by Sheridan [35] was utilized with minor adaptations. To define the material S-N behavior, Walker's mean stress correction to the Basquin equation, i.e., the Wohler curve, was used as seen in Eq. (1). Here, A and b represent the power-law coefficients of Basquin's law, $\Delta\sigma_{w0} = AN^b$. Eq. (1) was fit via linear regression to data corresponding to wrought 17-4, condition H1025, tested at R = -1.0 [66]. The loading ratio sensitivity constant, γ, was estimated according to Dowling's method for steels [67], as described by Eq. (2), assuming an ultimate strength of σ_u = 1195 MPa, drawn from prior testing of the material lot studied here [44]. When evaluated at N, $\Delta\sigma_{w0,N}$ represents the material's defect-free or 'plain' fatigue strength.

$$\Delta\sigma_{w0,N} = (1-R)AN^b\left(\frac{1-R}{2}\right)^{-\gamma} \tag{1}$$

$$\gamma = -0.0002S_u + 0.8818 \tag{2}$$

FCG properties were extracted from data pertaining to LPBF manufactured 17-4, condition H1025 [27]. Walker's mean-stress correction of Paris' law, Eq. (3), was fitted to crack growth rate data over multiple R values via multiple linear regression. C and m are the conventional power law coefficients for Paris's law and n the loading ratio correction factor. In this work, a correction factor, k, is added to allow for model tuning. The SIF term, $\Delta K = Y\Delta\sigma\sqrt{\pi a}$, is a function of the crack geometry factor Y, the applied stress range $\Delta\sigma$, and the crack size a. Integrating (3) by separation, with the limits of initial crack/defect size at 0 cycles to final crack size at N cycles results in Eq. (4), which is an expression for the initial defect size that grows to failure at N cycles, $a_{i,N}$. To perform this calculation, the final crack size a_f, was valued as 1.5 mm, based on the average apparent size of the fracture growth area in failed specimens, similar to the procedure used by Ref. [13].

$$\frac{da}{dN} = kC\left(\frac{\Delta K}{(1-R)^n}\right)^m \tag{3}$$

$$a_{i,N} = \left[a_f - N\left(1-\frac{m}{2}\right)k\left(\frac{C}{(1-R)^{nm}}\right)\left(Y\Delta\sigma\sqrt{\pi}\right)^n\right]^{\frac{1}{1-\frac{m}{2}}} \tag{4}$$

FCG behavior, expressed through $a_{i,N}$, was used to calculate the SIF range required to produce failure at the applied loading range and cycles, as in Eq. (5). All ΔK_N values less than ΔK_{th} were corrected to ΔK_{th}; this reasoning is detailed in Ref. [35]. ΔK_{th} was set equal to 4.06 MPa-m$^{1/2}$, drawn from Ref. [27]. The intermediate calculation of ΔK_N was used to calculate El-Haddad's intrinsic flaw size, $a_{0,N}$, for failure at N cycles, seen in Eq. (6). Finally, the result of FCG driven behavior was combined with S-N behavior through Eq. (7), the finite life El-Haddad model, which predicts the finite life fatigue limit, $\Delta\sigma_N$, in the presence of an existing defect of size, a_{eff}, at N cycles. The material constants and loading conditions utilized to construct the model are summarized in Table 5.

$$\Delta K_N = Y\Delta\sigma\sqrt{\pi a_{i,N}} \tag{5}$$

$$a_{0,N} = \frac{1}{\pi}\left(\frac{\Delta K_N}{Y\Delta\sigma}\right)^2 \tag{6}$$

$$\Delta\sigma_N = \Delta\sigma_{w0,N}\sqrt{\frac{a_{0,N}}{a_{eff} + a_{0,N}}} \tag{7}$$

Note that Eq. (4) and (6) utilize the stress term, $\Delta\sigma$, instead of $\Delta\sigma_{w0,N}$, as shown in Ref. [35]. This was done to provide a better physical representation of the testing scenario used in this paper. Sheridan's approach assumed that the initial ΔK value drives fatigue life and not the specific combination of stress and initial crack size. As such, Sheridan used the defect-free S-N relationship to calculate an equivalent initial flaw size that would result in the experimentally observed initial stress-intensity. In this way, Eq. (4) was reduced from a surface function of both stress and life to a curvilinear function of only fatigue life. Since only one stress value has been applied in the present work, the experimental stress has replaced $\Delta\sigma_{w0,N}$ which ensures that the observed defect size, a_{eff}, and the predicted defect size, $a_{i,N}$, match.

Table 5. Generalized finite life El-Haddad model parameters

Loading conditions				
R	σ_{max} *[MPa]*	$\Delta\sigma$ *[MPa]*		
0.1	867	780		
Stress-life parameters				
A [MPa]	*b*	γ		
1932	-0.071	0.6428		
FCG parameters				
C $\left[\frac{m/cycle}{(MPa-\sqrt{m})^m}\right]$	*m*	*n*	a_f *[m]*	*k*
4.4082×10^{-13}	4.2430	0.2448	0.0015	0.5

Figure 14(a) shows the results of the model, plotted along with the classical infinite life El-Haddad formulation, on a Kitagawa-Takahashi diagram. The classical model was defined using an infinite life endurance strength of $\Delta\sigma_{w0,\infty}$ = 765 MPa, drawn from Eq. (*1*) valued at R = 0.1, and ΔK_{th} = 4.06 MPa-m$^{1/2}$. The finite life model is illustrated as a series of curves representing cycles to failure at powers of 10, ranging from 10^4 to 10^7. These curves define the maximum initial flaw size allowable given a loading and life criteria, $\Delta\sigma_{service}$ & $N_{service}$. In a damage-tolerant or defect-tolerant design scenario, a non-destructive examination technique, such as XCT, could be used to establish the maximum allowable flaw size in a component, a_{allow}. This would be done by: (1) selecting a curve at $N_{service}$ cycles, (2) defining a y position along the curve knowing $\Delta\sigma_{service}$, and (3) extracting the associated x value, a_{allow}. The loading ratio, R, could also be selected.

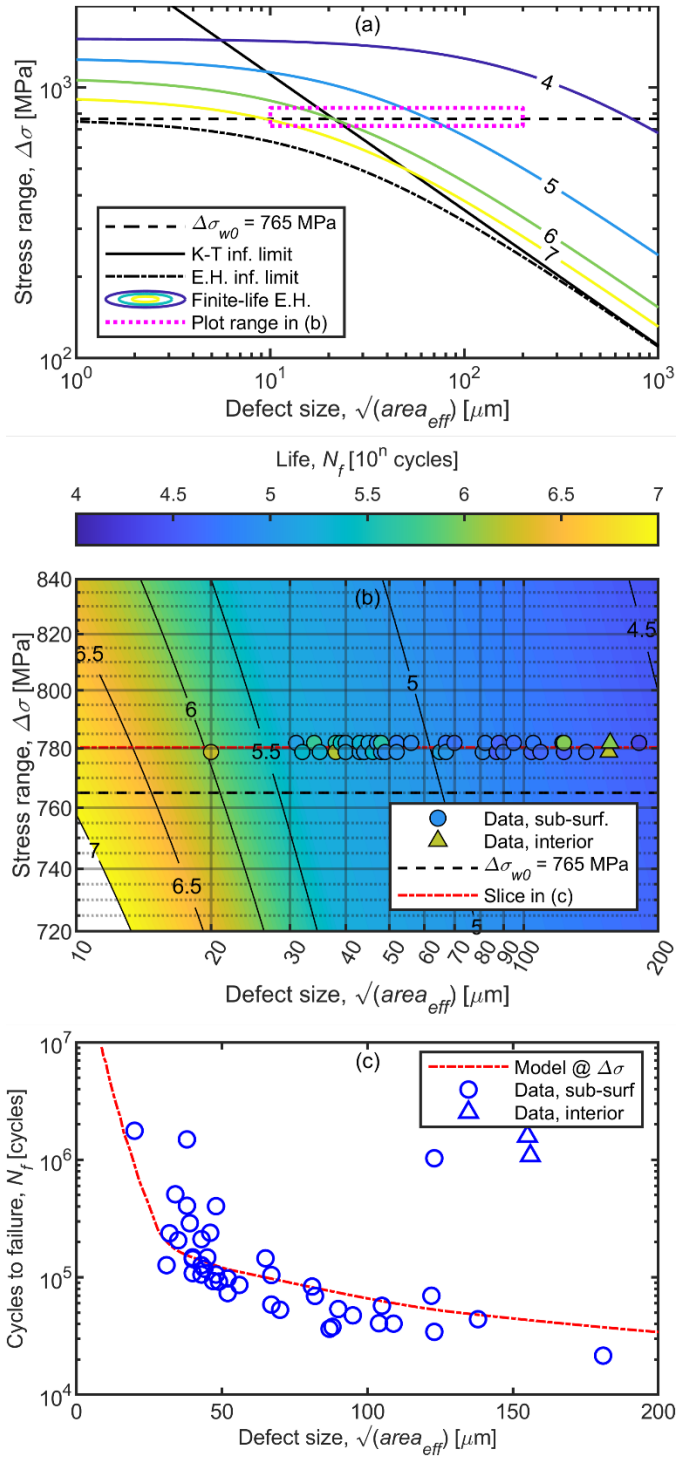

Figure 14. (a) Kitagawa-Takahashi diagram showing infinite finite life El-Haddad models. (b) Detailed region of (a), showing the model and experimental data. (c) A 'slice' of the model at Δσ = 780 MPa compared to experimental data.

Figure 14(b) also shows a region of (a) in detail, in addition to the experimental data acquired from the quantitative fractography analyses. Here, the model curves are colored in gradient, which maps to the predicted fatigue life. The data point infill coloring also maps to the same color scale – data point infill and background color matching indicates a good model fit. Note that the data have been slightly scattered about the nominal $\Delta\sigma$ value, in order to increase legibility. Figure 14(c) also assesses the fit of the model via a 'slice' of (b) at $\Delta\sigma$ = 780 MPa. In all plots, the correction factor, k, was set to a value of 0.5. This results in

an excellent fit to the data; error is generally within one half of one order of magnitude. Altering k, nominally set to 1, improved the fit likely due to the differences in short and long crack growth behavior. In general, further improvements to the model would focus on better modeling of short crack growth behavior, as current work has shown this contributes significantly to overall life, and these cracks can be complex, torturous in shape, and heterogenous in growth rate [37,45]. The data referenced to produce the Paris' law coefficient, C, is drawn from a FCG test where initial crack size was 6.0 mm whereas the present work evaluates cracks which had a final size of 1.5 mm. Notably, in both Figure 14(b-c) the two specimens with interior initiation sites, marked by triangular data points, depart significantly from the model. This is expected, as the model has been computed for sub-surface initiation behavior, and the result is a conservative miscalculation.

4.5. Fractography analyses

Some of the fracture surfaces with macro-scale features of note include that of specimen 1-1-A4, which displayed two initiation sites, shown in Figure 15. Specimen 1-1-A4 was low-life and located in the -Y region of the build plate, where specimens were typically associated with low-life. The prior presented XCT analyses established that these specimens had more pores and larger ones, which explains why this specimen showed two initiation sites. The relatively high porosity content increased the statistical likelihood that more than one pore of sufficient size, located near each other, would be in a critical sub-surface region. Figure 15(b-c) show the initiation sites which led to growth region #1 becoming a critical size, whereas growth region #2 was in an intermediate stage of growth prior to final failure.

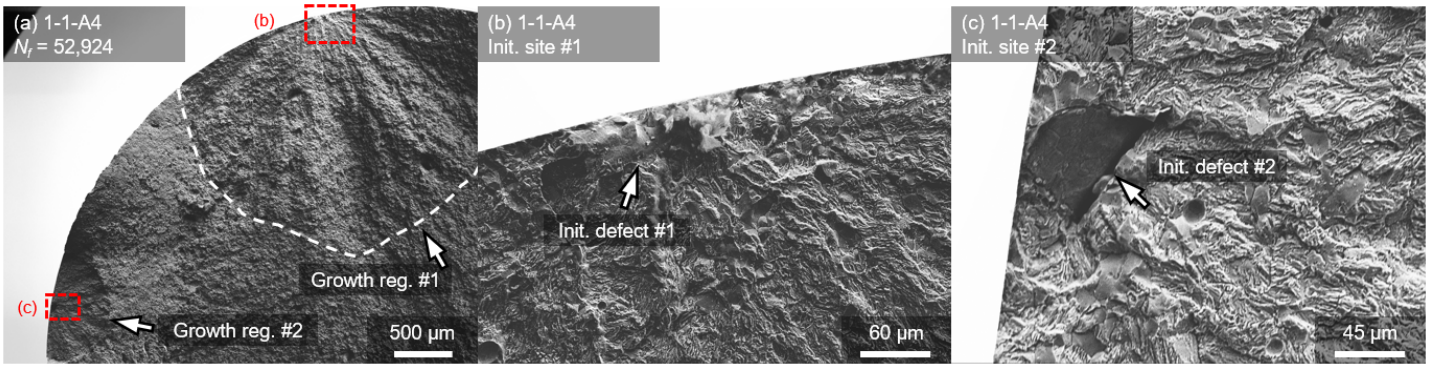

Figure 15. Specimen 1-1-A4 (Nf = 53,924) displaying (a) multiple fracture growth regions and (b-c) corresponding initiation sites.

Other specimens with atypical fracture surface features are 2-3-A1 and 3-1-A3, which had interior initiation sites, shown in Figure 16. Both specimens display defect groupings, seen in Figure 16(b) & (e), which are distanced in such a way to satisfy section 2.4, rule #3, but only barely so. As such, the defect size, $area_{eff}$, plotted in Figure 8 and Figure 14 may be overestimated, partly producing their outstanding nature on these plots. Figure 16(c) also shows what appears to be a transverse crack that grew in a region near to the initiating defects. It is not clear if these cracks emanated from a second unseen defect, or if they are the result of complex crack growth.

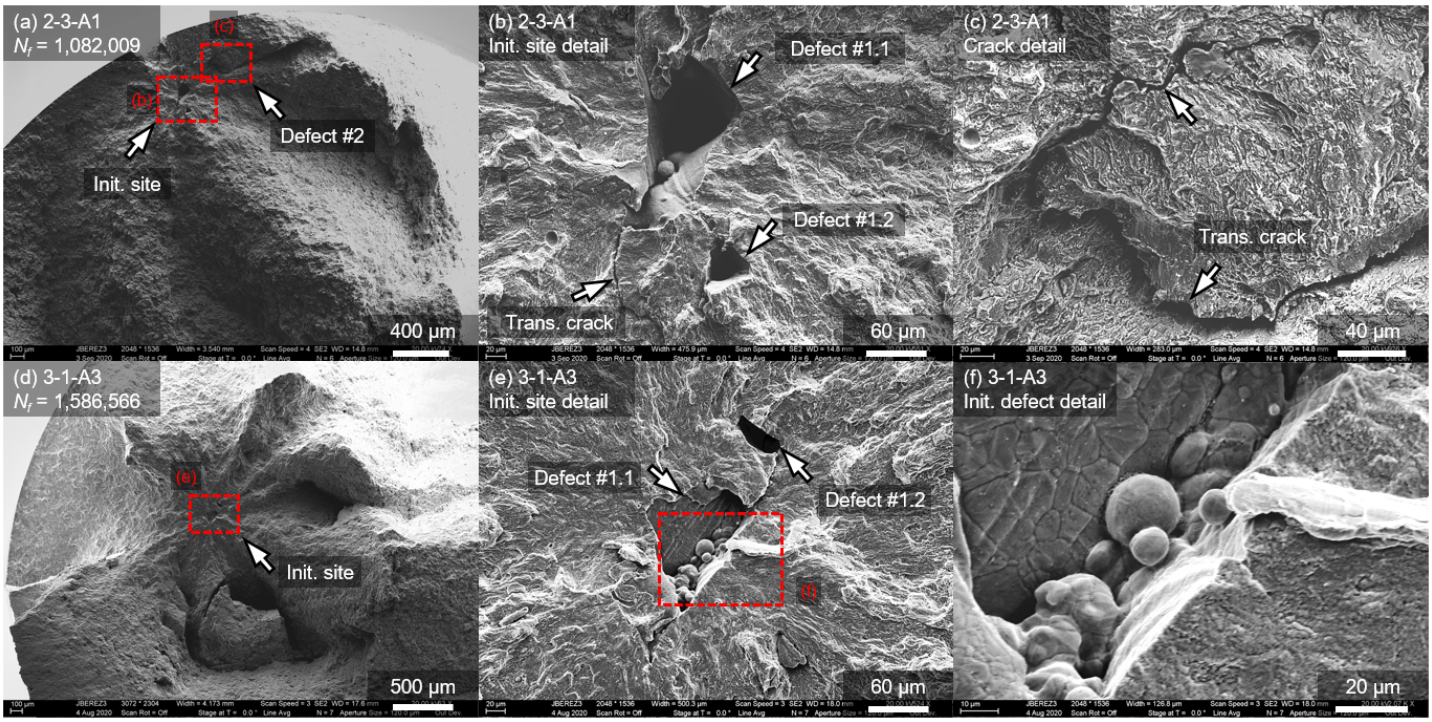

Figure 16. Specimens with interior initiation sites. (a-c) Specimen 2-2-A1 (N_f = 1,082,009). (d-f) Specimen 3-1-A3 (N_f = 1,586,566).

Notably, these specimens contained some of the largest observed defects, both approximately 115 µm in size, despite their long lives. If it is assumed that these specimen locations had a relatively low porosity levels similar to location 3-2, as was presented in the prior XCT analysis, the fundamental cause is the relatively small number of pores in total, and thus a lower statistical likelihood of their presence in the subsurface region. This led to the eventual selection of an interior site as the initiation location, despite the lower SIF associated with these defects as compared to sub-surface ones.

A selection of fracture initiating defects are shown in Figure 17, which displays defects from specimens with (a-c) low-, (d) intermediate-, (e) long-, and (f) very long-life spans. These fractographs were selected as being broadly representative of the size and nature of the LoF defects prevalent at each life span. The low-life span specimen LoF initiators in (a-c) all contain unfused powder particles, and range in size; a_{eff} = 181, 110, 67 µm, respectively. The smaller the defect, the longer the associated life of the specimen in these cases. The LoF defect in the intermediate-life specimen in (d), a_{eff} = 82 µm, like those in (a-c) has a generally complex morphology with some depth into the page, indicating these might be inter-layer LoF areas, as these were horizontally built specimens. Figure 17(e) shows a relatively small LoF defect, a_{eff} = 44 µm. Figure 17(f) shows a very small defect, a_{eff} = 38 µm. This small defect is torturous in shape but can still be identified a LoF defect via its subtly distinguished cellular texture, analogous to the other defects shown.

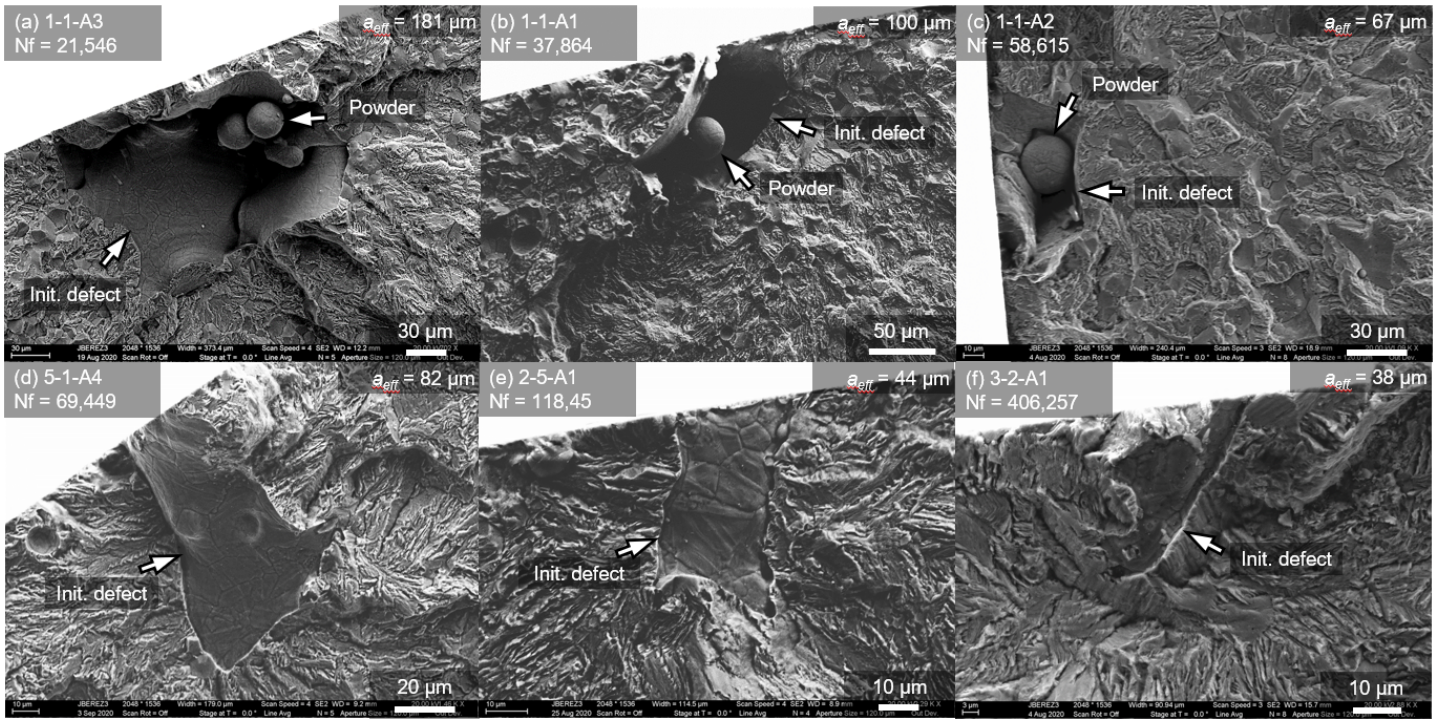

Figure 17. Selected fracture initiating defects from (a-c) low-, (d) intermediate-, (e) long-, and (f) very long-life span specimens.

Initiating defect size is not the only parameter that may contribute to fatigue life. Figure 18 displays fractographs from the fracture growth region of a low-life specimen, 1-2-A3. At low magnification, in Figure 18(a), it can be seen that the fracture growth path contains a number of visual anomalies that may be defects. The higher magnification fractographs show a sampling of these anomalies which are indeed LoF defects. These interior defects, while not large enough to have preferentially initiated fracture in a specimen with subsurface defects, nonetheless present local stress concentrations as well as regions where little to no energy is required to progress crack growth. Other work has attributed non-continuous crack growth rates to high defect density [68] and noted the tendency of defects near to the plane of crack growth to be included in the fracture path [37]. The observation of fatigue striations and their spacings in the areas around these defects would support this understanding, but high strength steels such as 17-4 are known not to display these striations, such as are seen in aluminum alloys [69].

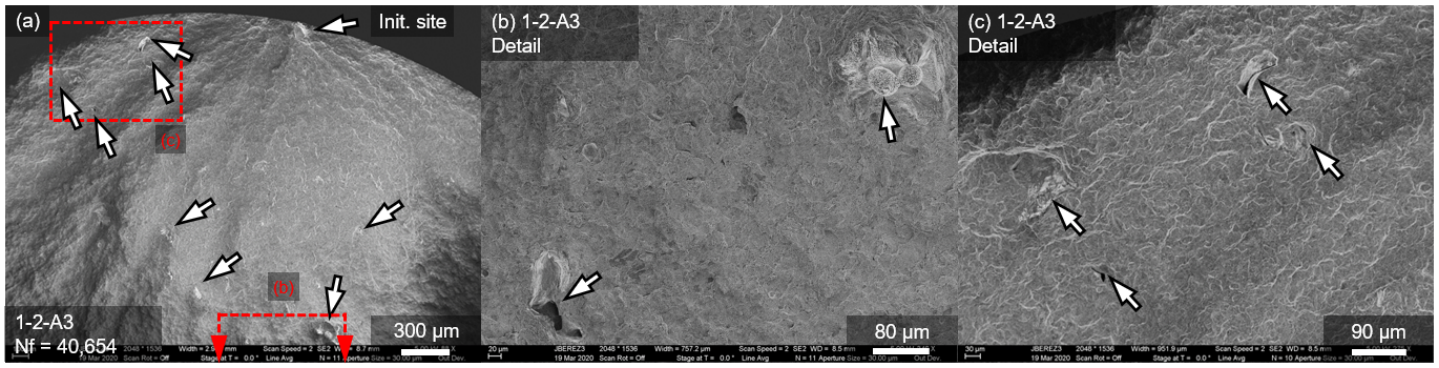

Figure 18. Low-life specimen displaying a high density of defects in the fracture growth path.

5. Conclusions

Current research has generally focused on LPBF process parameters such as material feedstock quality, laser processing parameters, build/scan strategy, and post-processing in an effort to control end-component quality. Through the present work, it has been shown that components with these process parameters held constant still exhibit significant variation in their volumetric defect content and fatigue behavior. Production-scale implementations of LPBF processes thus currently face a two-fold challenge in producing high quality parts with repeatable properties. The first challenge is process measurement and control; the localized defect trends of an LPBF system and total span of end-component quality variation must be identified thereby allowing part location and build density to be controlled. This work has elucidated this through a rigorous probabilistic description of life. The second challenge is qualification; under the assumption that defect content will vary, parts must be screened for defects against relevant acceptance criteria. Such criteria could be established via the finite life El-Haddad model, which this work has proven the application of. A summary of the present work is presented through the conclusions enumerated below.

1. A production-scale implementation of the LPBF process produced components with highly variant fatigue lives. This variability can be attributed to the component specific porosity content, which varied over locations of the build volume.
2. Quantitative fractography revealed that large sub-surface LoF defects led to lower fatigue lives in nearly all cases. The likelihood of such a defect increased in components with more overall defects.
3. LPBF process byproducts, such as condensate and spatter, were likely the cause of increased LoF porosity in the downstream gas flow region of the build volume.
4. The highly variant fatigue lives were well-modelled by a fitted lognormal distribution, which may serve a strong safe-life approach design tool, predicting probability of failure as a function of cycle count.
5. A damage-tolerant approach, in the form of a finite life El-Haddad model, was applied to accurately predict component life as a function of equivalent initial flaw size.

CRediT authorship contribution statement

Jaime Berez: Writing – original draft, writing – review & editing, conceptualization, methodology, investigation, formal analysis, visualization, software, data curation. **Luke Sheridan:** Writing – review and editing, formal analysis, software. **Christopher Saldaña:** Writing – review & editing, conceptualization, supervision, project administration, funding acquisition.

Acknowledgements

This work was supported in part by the Department of Energy [DE-EE0008303]; and the National Science Foundation [CMMI-1825640]. The authors would like to acknowledge the staff of Delta TechOps (R. Ramakrishnan, V.S.K Adapa, J. Mallory, D. Crear, and J. Robertson) for their assistance with this work. E. Jost is acknowledged for their feedback on earlier versions of this manuscript.

References

[1] M. Schmidt, M. Merklein, D. Bourell, D. Dimitrov, T. Hausotte, K. Wegener, L. Overmeyer, F. Vollertsen, G.N. Levy, Laser based additive manufacturing in industry and academia, CIRP Annals. 66 (2017) 561–583. https://doi.org/10.1016/j.cirp.2017.05.011.

[2] I. Gibson, D.W. Rosen, B. Stucker, Powder Bed Fusion Processes, in: I. Gibson, D.W. Rosen, B. Stucker (Eds.), Additive Manufacturing Technologies, Springer US, Boston, MA, 2010: pp. 120–159. https://doi.org/10.1007/978-1-4419-1120-9_5.

[3] M. Kamal, G. Rizza, Design for metal additive manufacturing for aerospace applications, in: Additive Manufacturing for the Aerospace Industry, Elsevier, 2019: pp. 67–86. https://doi.org/10.1016/B978-0-12-814062-8.00005-4.

[4] D. Bourell, J.P. Kruth, M. Leu, G. Levy, D. Rosen, A.M. Beese, A. Clare, Materials for additive manufacturing, CIRP Annals. 66 (2017) 659–681. https://doi.org/10.1016/j.cirp.2017.05.009.

[5] P.H. Wirsching, NASA Contractor Report 3697: Statistical Summaries of Fatigue Data for Design Purposes, (1983).

[6] J. Schijve, Fatigue of structures and materials, Second edition, Springer, Dordrecht, 2009.

[7] Y. Murakami, S. Beretta, Small Defects and Inhomogeneities in Fatigue Strength: Experiments, Models and Statistical Implications, Extremes. 2 (1999) 123–147. https://doi.org/10.1023/A:1009976418553.

[8] C. Przybyla, R. Prasannavenkatesan, N. Salajegheh, D.L. McDowell, Microstructure-sensitive modeling of high cycle fatigue, International Journal of Fatigue. 32 (2010) 512–525. https://doi.org/10.1016/j.ijfatigue.2009.03.021.

[9] N. Shamsaei, A. Yadollahi, L. Bian, S.M. Thompson, An overview of Direct Laser Deposition for additive manufacturing; Part II: Mechanical behavior, process parameter optimization and control, Additive Manufacturing. 8 (2015) 12–35. https://doi.org/10.1016/j.addma.2015.07.002.

[10] M. Seifi, A. Salem, J. Beuth, O. Harrysson, J.J. Lewandowski, Overview of Materials Qualification Needs for Metal Additive Manufacturing, JOM. 68 (2016) 747–764. https://doi.org/10.1007/s11837-015-1810-0.
[11] A. Yadollahi, N. Shamsaei, Additive manufacturing of fatigue resistant materials: Challenges and opportunities, International Journal of Fatigue. 98 (2017) 14–31. https://doi.org/10.1016/j.ijfatigue.2017.01.001.
[12] S. Beretta, S. Romano, A comparison of fatigue strength sensitivity to defects for materials manufactured by AM or traditional processes, International Journal of Fatigue. 94 (2017) 178–191. https://doi.org/10.1016/j.ijfatigue.2016.06.020.
[13] S. Beretta, M. Gargourimotlagh, S. Foletti, A. du Plessis, M. Riccio, Fatigue strength assessment of "as built" AlSi10Mg manufactured by SLM with different build orientations, International Journal of Fatigue. 139 (2020) 105737. https://doi.org/10.1016/j.ijfatigue.2020.105737.
[14] A. Yadollahi, M.J. Mahtabi, A. Khalili, H.R. Doude, J.C. Newman, Fatigue life prediction of additively manufactured material: Effects of surface roughness, defect size, and shape, Fatigue Fract Eng Mater Struct. 41 (2018) 1602–1614. https://doi.org/10.1111/ffe.12799.
[15] H. Masuo, Y. Tanaka, S. Morokoshi, H. Yagura, T. Uchida, Y. Yamamoto, Y. Murakami, Influence of defects, surface roughness and HIP on the fatigue strength of Ti-6Al-4V manufactured by additive manufacturing, International Journal of Fatigue. 117 (2018) 163–179. https://doi.org/10.1016/j.ijfatigue.2018.07.020.
[16] P.D. Nezhadfar, R. Shrestha, N. Phan, N. Shamsaei, Fatigue behavior of additively manufactured 17-4 PH stainless steel: Synergistic effects of surface roughness and heat treatment, International Journal of Fatigue. 124 (2019) 188–204. https://doi.org/10.1016/j.ijfatigue.2019.02.039.
[17] B. Torries, A. Imandoust, S. Beretta, S. Shao, N. Shamsaei, Overview on Microstructure- and Defect-Sensitive Fatigue Modeling of Additively Manufactured Materials, JOM. 70 (2018) 1853–1862. https://doi.org/10.1007/s11837-018-2987-9.
[18] O. Scott-Emuakpor, C. Holycross, T. George, K. Knapp, J. Beck, Fatigue and Strength Studies of Titanium 6Al–4V Fabricated by Direct Metal Laser Sintering, Journal of Engineering for Gas Turbines and Power. 138 (2016) 022101. https://doi.org/10.1115/1.4031271.
[19] F.H. Kim, S.P. Moylan, Literature review of metal additive manufacturing defects, National Institute of Standards and Technology, Gaithersburg, MD, 2018. https://doi.org/10.6028/NIST.AMS.100-16.
[20] S.M.H. Hojjatzadeh, N.D. Parab, Q. Guo, M. Qu, L. Xiong, C. Zhao, L.I. Escano, K. Fezzaa, W. Everhart, T. Sun, L. Chen, Direct observation of pore formation mechanisms during LPBF additive manufacturing process and high energy density laser welding, International Journal of Machine Tools and Manufacture. 153 (2020) 103555. https://doi.org/10.1016/j.ijmachtools.2020.103555.
[21] A.A. Martin, N.P. Calta, S.A. Khairallah, J. Wang, P.J. Depond, A.Y. Fong, V. Thampy, G.M. Guss, A.M. Kiss, K.H. Stone, C.J. Tassone, J. Nelson Weker, M.F. Toney, T. van Buuren, M.J. Matthews, Dynamics of pore formation during laser powder bed fusion additive manufacturing, Nat Commun. 10 (2019) 1987. https://doi.org/10.1038/s41467-019-10009-2.
[22] D.L. McDowell, Basic issues in the mechanics of high cycle metal fatigue, Int J Fract. 80 (1996) 103–145. https://doi.org/10.1007/BF00012666.
[23] P.D. Nezhadfar, K. Anderson-Wedge, S.R. Daniewicz, N. Phan, S. Shao, N. Shamsaei, Improved high cycle fatigue performance of additively manufactured 17-4 PH stainless steel via in-process refining micro-/defect-structure, Additive Manufacturing. 36 (2020) 101604. https://doi.org/10.1016/j.addma.2020.101604.
[24] J. Gumpinger, A.D. Brandão, E. Beevers, T. Rohr, T. Ghidini, S. Beretta, S. Romano, Expression of Additive Manufacturing Surface Irregularities through a Flaw-Based Assessment, in: N. Shamsaei, S. Daniewicz, N. Hrabe, S. Beretta, J. Waller, M. Seifi (Eds.), Structural Integrity of Additive Manufactured Parts, ASTM International, 100 Barr Harbor Drive, PO Box C700, West Conshohocken, PA 19428-2959, 2020: pp. 234–249. https://doi.org/10.1520/STP162020180098.
[25] S. Romano, A. Brückner-Foit, A. Brandão, J. Gumpinger, T. Ghidini, S. Beretta, Fatigue properties of AlSi10Mg obtained by additive manufacturing: Defect-based modelling and prediction of fatigue strength, Engineering Fracture Mechanics. 187 (2018) 165–189. https://doi.org/10.1016/j.engfracmech.2017.11.002.
[26] S. Romano, S. Miccoli, S. Beretta, A new FE post-processor for probabilistic fatigue assessment in the presence of defects and its application to AM parts, International Journal of Fatigue. 125 (2019) 324–341. https://doi.org/10.1016/j.ijfatigue.2019.04.008.
[27] S. Romano, P.D. Nezhadfar, N. Shamsaei, M. Seifi, S. Beretta, High cycle fatigue behavior and life prediction for additively manufactured 17-4 PH stainless steel: Effect of sub-surface porosity and surface roughness, Theoretical and Applied Fracture Mechanics. 106 (2020). https://doi.org/10.1016/j.tafmec.2020.102477.
[28] S. Beretta, Y. Murakami, STATISTICAL ANALYSIS OF DEFECTS FOR FATIGUE STRENGTH PREDICTION AND QUALITY CONTROL OF MATERIALS, Fat Frac Eng Mat Struct. 21 (1998) 1049–1065. https://doi.org/10.1046/j.1460-2695.1998.00104.x.
[29] H. Kitagawa, S. Takahashi, Application of fracture mechanics to very small cracks or the cracks in the early stage, in: 1976: pp. 627–630.
[30] M.H. El-Haddad, T.H. Topper, K.N. Smith, Prediction of non propagating cracks, Engineering Fracture Mechanics. 11 (1979) 573–584. https://doi.org/10.1016/0013-7944(79)90081-X.
[31] Y. Murakami, M. Endo, Effects of defects, inclusions and inhomogeneities on fatigue strength, International Journal of Fatigue. 16 (1994) 163–182. https://doi.org/10.1016/0142-1123(94)90001-9.
[32] Y.N. Hu, S.C. Wu, P.J. Withers, J. Zhang, H.Y.X. Bao, Y.N. Fu, G.Z. Kang, The effect of manufacturing defects on the fatigue life of selective laser melted Ti-6Al-4V structures, Materials & Design. 192 (2020) 108708. https://doi.org/10.1016/j.matdes.2020.108708.
[33] Z. Wu, S. Wu, J. Bao, W. Qian, S. Karabal, W. Sun, P.J. Withers, The effect of defect population on the anisotropic fatigue resistance of AlSi10Mg alloy fabricated by laser powder bed fusion, International Journal of Fatigue. 151 (2021) 106317. https://doi.org/10.1016/j.ijfatigue.2021.106317.
[34] M. Ciavarella, F. Monno, On the possible generalizations of the Kitagawa–Takahashi diagram and of the El Haddad equation to finite life, International Journal of Fatigue. 28 (2006) 1826–1837. https://doi.org/10.1016/j.ijfatigue.2005.12.001.
[35] L. Sheridan, A modified El-Haddad model for versatile defect tolerant design, International Journal of Fatigue. 145 (2021) 106062. https://doi.org/10.1016/j.ijfatigue.2020.106062.
[36] A. Yadollahi, M. Mahmoudi, A. Elwany, H. Doude, L. Bian, J.C. Newman, Fatigue-life prediction of additively manufactured material: Effects of heat treatment and build orientation, Fatigue Fract Eng Mater Struct. 43 (2020) 831–844. https://doi.org/10.1111/ffe.13200.
[37] W. Qian, S. Wu, Z. Wu, S. Ahmed, W. Zhang, G. Qian, P.J. Withers, In situ X-ray imaging of fatigue crack growth from multiple defects in additively manufactured AlSi10Mg alloy, International Journal of Fatigue. 155 (2022) 106616. https://doi.org/10.1016/j.ijfatigue.2021.106616.
[38] L. Sheridan, O.E. Scott-Emuakpor, T. George, J.E. Gockel, Relating porosity to fatigue failure in additively manufactured alloy 718, Materials Science and Engineering: A. 727 (2018) 170–176. https://doi.org/10.1016/j.msea.2018.04.075.
[39] S. Romano, A. Brandao, J. Gumpinger, M. Gschweitl, S. Beretta, Qualification of AM parts: Extreme value statistics applied to tomographic measurements, Materials and Design. 131 (2017) 32–48. https://doi.org/10.1016/j.matdes.2017.05.091.

[40] M. Tiryakioğlu, On the relationship between statistical distributions of defect size and fatigue life in 7050-T7451 thick plate and A356-T6 castings, Materials Science and Engineering: A. 520 (2009) 114–120. https://doi.org/10.1016/j.msea.2009.05.005.
[41] N.M. Heckman, T.A. Ivanoff, A.M. Roach, B.H. Jared, D.J. Tung, H.J. Brown-Shaklee, T. Huber, D.J. Saiz, J.R. Koepke, J.M. Rodelas, J.D. Madison, B.C. Salzbrenner, L.P. Swiler, R.E. Jones, B.L. Boyce, Automated high-throughput tensile testing reveals stochastic process parameter sensitivity, Materials Science and Engineering: A. 772 (2020) 138632. https://doi.org/10.1016/j.msea.2019.138632.
[42] P. Li, D.H. Warner, J.W. Pegues, M.D. Roach, N. Shamsaei, N. Phan, Towards predicting differences in fatigue performance of laser powder bed fused Ti-6Al-4V coupons from the same build, International Journal of Fatigue. 126 (2019) 284–296. https://doi.org/10.1016/j.ijfatigue.2019.05.004.
[43] A. Soltani-Tehrani, J. Pegues, N. Shamsaei, Fatigue Behavior of Additively Manufactured 17-4 PH Stainless Steel: The Effects of Part Location and Powder Re-use, Additive Manufacturing. (2020). https://doi.org/10.1016/j.addma.2020.101398.
[44] J. Berez, C. Saldana, Fatigue of laser powder bed fusion processed 17-4 stainless steel using prior process exposed powder feedstock, Journal of Manufacturing Processes. 71 (2021) 515–527. https://doi.org/10.1016/j.jmapro.2021.09.045.
[45] P. Ravi, D. Naragani, P. Kenesei, J.-S. Park, M.D. Sangid, Direct observations and characterization of crack closure during microstructurally small fatigue crack growth via in-situ high-energy X-ray characterization, Acta Materialia. 205 (2021) 116564. https://doi.org/10.1016/j.actamat.2020.116564.
[46] Z.A. Young, Q. Guo, N.D. Parab, C. Zhao, M. Qu, L.I. Escano, K. Fezzaa, W. Everhart, T. Sun, L. Chen, Types of spatter and their features and formation mechanisms in laser powder bed fusion additive manufacturing process, Additive Manufacturing. 36 (2020) 101438. https://doi.org/10.1016/j.addma.2020.101438.
[47] A.T. Sutton, C.S. Kriewall, M.C. Leu, J.W. Newkirk, Powders for Additive Manufacturing Processes: Characterization Techniques and Effects on Part Properties, (n.d.) 27.
[48] C. Rock, Analysis of Self-Organized Patterned Surface Oxide Spots on Ejected Spatter Produced during Laser Powder Bed Fusion, Additive Manufacturing. (2020) 10.
[49] Q. Guo, C. Zhao, L.I. Escano, Z. Young, L. Xiong, K. Fezzaa, W. Everhart, B. Brown, T. Sun, L. Chen, Transient dynamics of powder spattering in laser powder bed fusion additive manufacturing process revealed by in-situ high-speed high-energy x-ray imaging, Acta Materialia. 151 (2018) 169–180. https://doi.org/10.1016/j.actamat.2018.03.036.
[50] M. Simonelli, C. Tuck, N.T. Aboulkhair, I. Maskery, I. Ashcroft, R.D. Wildman, R. Hague, A Study on the Laser Spatter and the Oxidation Reactions During Selective Laser Melting of 316L Stainless Steel, Al-Si10-Mg, and Ti-6Al-4V, Metall and Mat Trans A. 46 (2015) 3842–3851. https://doi.org/10.1007/s11661-015-2882-8.
[51] M.J. Heiden, L.A. Deibler, J.M. Rodelas, J.R. Koepke, D.J. Tung, D.J. Saiz, B.H. Jared, Evolution of 316L stainless steel feedstock due to laser powder bed fusion process, Additive Manufacturing. 25 (2019) 84–103. https://doi.org/10.1016/j.addma.2018.10.019.
[52] J. Reijonen, A. Revuelta, T. Riipinen, K. Ruusuvuori, P. Puukko, On the effect of shielding gas flow on porosity and melt pool geometry in laser powder bed fusion additive manufacturing, Additive Manufacturing. 32 (2020) 101030. https://doi.org/10.1016/j.addma.2019.101030.
[53] R. Esmaeilizadeh, U. Ali, A. Keshavarzkermani, Y. Mahmoodkhani, E. Marzbanrad, E. Toyserkani, On the effect of spatter particles distribution on the quality of Hastelloy X parts made by laser powder-bed fusion additive manufacturing, Journal of Manufacturing Processes. 37 (2019) 11–20. https://doi.org/10.1016/j.jmapro.2018.11.012.
[54] A. Ladewig, G. Schlick, M. Fisser, V. Schulze, U. Glatzel, Influence of the shielding gas flow on the removal of process by-products in the selective laser melting process, Additive Manufacturing. 10 (2016) 1–9. https://doi.org/10.1016/j.addma.2016.01.004.
[55] A.B. Anwar, Q.-C. Pham, Study of the spatter distribution on the powder bed during selective laser melting, Additive Manufacturing. 22 (2018) 86–97. https://doi.org/10.1016/j.addma.2018.04.036.
[56] T.P. Moran, D.H. Warner, A. Soltani-Tehrani, N. Shamsaei, N. Phan, Spatial inhomogeneity of build defects across the build plate in laser powder bed fusion, Additive Manufacturing. 47 (2021) 102333. https://doi.org/10.1016/j.addma.2021.102333.
[57] A.B. Anwar, Q.-C. Pham, Selective laser melting of AlSi10Mg: Effects of scan direction, part placement and inert gas flow velocity on tensile strength, Journal of Materials Processing Technology. 240 (2017) 388–396. https://doi.org/10.1016/j.jmatprotec.2016.10.015.
[58] C. Li, S. Wu, J. Zhang, L. Xie, Y. Zhang, Determination of the fatigue P-S-N curves – A critical review and improved backward statistical inference method, International Journal of Fatigue. 139 (2020) 105789. https://doi.org/10.1016/j.ijfatigue.2020.105789.
[59] Y. Murakami, T. Takagi, K. Wada, H. Matsunaga, Essential structure of S-N curve: Prediction of fatigue life and fatigue limit of defective materials and nature of scatter, International Journal of Fatigue. 146 (2021) 106138. https://doi.org/10.1016/j.ijfatigue.2020.106138.
[60] S.S. Wilks, The Large-Sample Distribution of the Likelihood Ratio for Testing Composite Hypotheses, Ann. Math. Statist. 9 (1938) 60–62. https://doi.org/10.1214/aoms/1177732360.
[61] I.J. Myung, Tutorial on maximum likelihood estimation, Journal of Mathematical Psychology. 47 (2003) 90–100. https://doi.org/10.1016/S0022-2496(02)00028-7.
[62] Y. Wu, P.H. Wirsching, Advanced Reliability Method for Fatigue Analysis, Journal of Engineering Mechanics. 110 (1984) 536–553. https://doi.org/10.1061/(ASCE)0733-9399(1984)110:4(536).
[63] A. Brot, Weibull or Log-Normal Distribution to Characterize Fatigue Life Scatter – Which Is More Suitable?, in: A. Niepokolczycki, J. Komorowski (Eds.), ICAF 2019 – Structural Integrity in the Age of Additive Manufacturing, Springer International Publishing, Cham, 2020: pp. 551–561. https://doi.org/10.1007/978-3-030-21503-3_44.
[64] W. Weibull, A Statistical Distribution Function of Wide Applicability, ASME Journal of Applied Mechanics. (1951) 293–297.
[65] P.H. Wirsching, Fatigue reliability, Prog. Struct. Engng. Mater. 1 (1998) 200–206. https://doi.org/10.1002/pse.2260010213.
[66] D. Nie, Y. Mutoh, Fatigue Limit Prediction of the Matrix of 17-4PH Stainless Steel Based on Small Crack Mechanics, Journal of Pressure Vessel Technology. 135 (2013) 021407. https://doi.org/10.1115/1.4023428.
[67] N.E. Dowling, C.A. Calhoun, A. Arcari, Mean stress effects in stress-life fatigue and the Walker equation, Fatigue & Fracture of Engineering Materials & Structures. 32 (2009) 163–179. https://doi.org/10.1111/j.1460-2695.2008.01322.x.
[68] A. Yadollahi, Effects of crack orientation and heat treatment on fatigue-crack-growth behavior of AM 17-4 PH stainless steel, Engineering Fracture Mechanics. (2020) 17.
[69] R.A. Lund, Fatigue Fracture Appearances, in: B.A. Miller, R.J. Shipley, R.J. Parrington, D.P. Dennies (Eds.), ASM Handbook Volume 11: Failure Analysis and Prevention, ASM, 2021.